Journal of Biomolecular NMR (2018) 70:93–102
https://doi.org/10.1007/s10858-017-0161-2

ARTICLE

A new class of CEST experiment based on selecting different magnetization components at the start and end of the CEST relaxation element: an application to ^{1}H CEST

Tairan Yuwen[1] · **Lewis E. Kay**[1,2]

Received: 13 November 2017 / Accepted: 22 December 2017 / Published online: 19 January 2018

Abstract
Chemical exchange saturation transfer (CEST) experiments are becoming increasingly popular for investigating biomolecular exchange dynamics with rates on the order of approximately 50–500 s^{-1} and a rich toolkit of different methods has emerged over the past few years. Typically, experiments are based on the evolution of longitudinal magnetization, or in some cases two-spin order, during a fixed CEST relaxation delay, with the same class of magnetization prepared at the start and selected at end of the CEST period. Here we present a pair of TROSY-based pulse schemes for recording amide and methyl ^{1}H CEST profiles where longitudinal magnetization at the start evolves to produce two-spin order that is then selected at the completion of the CEST element. This selection process subtracts out contributions from ^{1}H–^{1}H cross-relaxation on the fly that would otherwise complicate analysis of the data. It also obviates the need to record spin-state selective CEST profiles as an alternative to eliminating NOE effects, leading to significant improvements in sensitivity. The utility of the approach is demonstrated on a sample of a cavity mutant of T4 lysozyme that undergoes chemical exchange between conformations where the cavity is free and occupied.

Keywords Chemical exchange · ^{1}H CEST · NOE dips · Longitudinal order · TROSY

Introduction

Although the underlying theory behind chemical exchange saturation transfer (CEST) based experiments was presented over a half a century ago (Forsen and Hoffman 1963), interesting new nuances of this simple experiment are still being discovered that have important practical applications. Unlike the more popular relaxation dispersion class of experiment where the effects of chemical exchange are monitored by the decay of transverse magnetization (Palmer et al. 2001), CEST experiments (Vallurupalli et al. 2017) or their related DEST counterparts (Fawzi et al. 2011) focus on longitudinal magnetization that decays much more slowly in applications involving macromolecules. As a result CEST/DEST is ideally suited for studies of relatively slow exchange processes with exchange rates typically on the order of 50–500 s^{-1}. Initial CEST experiments for measuring chemical shifts of rare (so called excited) states, that typically cannot be observed directly in standard NMR experiments, focused on ^{15}N magnetization (Vallurupalli et al. 2012) or in cases where ^{13}C could be added at selected sites, on ^{13}C magnetization (Bouvignies and Kay 2012a; Hansen et al. 2013; Rennella et al. 2015). Notably, it was realized shortly thereafter that applications could be carried out on uniformly ^{15}N- and ^{13}C-labeled proteins with little complication from the significant one-bond ^{13}C–^{13}C scalar couplings (Vallurupalli et al. 2013) that are so deleterious in dispersion studies (Ishima et al. 2004), opening the possibility of recording ^{13}C chemical shifts of excited state conformers at a large number of side-chain positions (Bouvignies et al. 2014). Studies using ^{1}H CEST based experiments have been more limited, fraught with artifacts that derive from NOE-based magnetization

Electronic supplementary material The online version of this article (https://doi.org/10.1007/s10858-017-0161-2) contains supplementary material, which is available to authorized users.

✉ Lewis E. Kay
kay@pound.med.utoronto.ca

[1] Departments of Molecular Genetics, Biochemistry and Chemistry, University of Toronto, Toronto, ON M5S 1A8, Canada

[2] Program in Molecular Medicine, The Hospital for Sick Children Research Institute, Toronto, ON M5G 0A4, Canada

transfer that are difficult to separate from chemical exchange based signals (Bouvignies and Kay 2012b). Yet, even in this case, chemical and dipolar exchange processes can be separated, by subtracting ^{1}H CEST profiles recorded for each spin-state of the attached ^{15}N or ^{13}C heteroatom (Yuwen et al. 2017a, b; Yuwen and Kay 2017).

All of the biomolecular CEST experiments that are known to us select magnetization at the end of the CEST period that is of the same form as that prepared immediately prior to it (for example, in most cases longitudinal magnetization). However, in some cases significant sensitivity gains can be realized by selecting different elements, such as longitudinal magnetization and longitudinal order at the start and end of the CEST relaxation period, respectively. Herein we describe one such set of applications that focuses on ^{1}H CEST. We show that NOE-based exchange processes can be eliminated using this new approach in a series of studies involving a T4 lysozyme exchanging system (Bouvignies et al. 2011; Mulder et al. 2001) as an illustration.

Materials and methods

Sample preparation

An NMR sample of [U-^{15}N; U-^{2}H] T4 lysozyme where Leu is replaced by Ala at position 99, L99A T4L, was prepared following the protocol described by Bouvignies et al. (2011), with 1.5 mM protein dissolved in 50 mM sodium phosphate, 25 mM NaCl, 2 mM EDTA, 2 mM NaN_3, pH 5.5, 90%H_2O/10%D_2O. A 1.7 mM [U-^{15}N; U-^{2}H; Ileδ1-$^{13}CH_3$; Leu,Val-$^{13}CH_3$/$^{12}CD_3$; Met-$^{13}CH_3$] L99A T4L sample was generated similarly with the final buffer 100% D_2O. The level of deuteration in all samples was > 95% at all carbon sites.

NMR spectroscopy

All ^{1}H CEST experiments were recorded on L99A T4L samples at 8.8 °C using an 800 MHz Avance III Bruker spectrometer equipped with a cryogenically cooled probe. Amide ^{1}H CEST datasets were measured using a [U-^{15}N; U-^{2}H]-labeled L99A T4L sample (pulse scheme of Fig. 2a) with a weak B_1 field of 30.4 Hz and T_{Ex} = 400 ms. Experiments were obtained by varying the position of the ^{1}H CEST field from 6.2 to 9.4 ppm with a step-size of 30 Hz (one 2D dataset for each frequency position). In addition, a regular ^{1}H–^{15}N HSQC spectrum was recorded as the 2D reference dataset with intensities in the CEST profile subsequently normalized relative to corresponding peak intensities in the HSQC. Each 2D plane was recorded with four transients/FID, a relaxation delay of 0.5 s and (768, 56) complex points in (t_2, t_1) to give a net acquisition time of ~ 7 min/spectrum and a net measurement time for each pseudo-3D CEST dataset of ~ 11 h. By means of comparison spin-state selective ^{1}H CEST experiments were also recorded, obtained as interleaved pseudo-4D datasets, by collecting a pair of components corresponding to I_zN^{α} and I_zN^{β} magnetization transfer pathways, see below (Yuwen et al. 2017b) All parameters were the same between each of the different classes of experiment with the exception that two transients were measured for each spin-state selective FID so that the total amount of measurement time of the complete datasets was the same.

^{1}H methyl-TROSY based CEST experiments were measured using a [U-^{15}N; U-^{2}H; Ileδ1-$^{13}CH_3$; Leu,Val-$^{13}CH_3$/$^{12}CD_3$; Met-$^{13}CH_3$]-labeled L99A T4L sample with the pulse scheme of Fig. 2b, a weak B_1 field of 30.6 Hz and T_{Ex} = 500 ms. The position of the ^{1}H CEST field was varied from − 1.0 to 2.2 ppm with a step size of 30 Hz and a reference ^{1}H–^{13}C HMQC dataset was recorded as well. Each 2D dataset was obtained with four transients/FID, a relaxation delay of 1.0 s and (768, 32) complex points in (t_2, t_1) to give a net acquisition time of ~ 6 min/spectrum and a net measurement time for each pseudo-3D CEST dataset of ~ 10 h. Spin-state selective methyl ^{1}H CEST experiments were also recorded, measured as interleaved pseudo-4D datasets (Yuwen et al. 2017a), with two transients/FID so that the total measurement time for all experiments was identical.

Data analysis

All NMR spectra were processed and analyzed using the *NMRPipe* suite of programs (Delaglio et al. 1995), with peak intensities extracted with the *autofit* subroutine. Analysis of the CEST profiles was carried out using the software package *ChemEx* (https://github.com/gbouvignies/chemex), with a separate module for fitting the ^{1}H profiles that is available from the authors upon request. ^{1}H CEST difference profiles were obtained directly from the spectra recorded using the schemes of Fig. 2 with no manipulation of datasets required. The spin-state selective profiles where obtained as described previously (Yuwen et al. 2017b), with difference CEST profiles generated from subtraction of the two corresponding spin-state selective traces. In total 52(8) amide(methyl) ^{1}H CEST profiles were selected and analyzed to extract chemical shift differences (ppm) between corresponding spins in the ground (G) and excited (E) states, $\Delta\varpi_{GE}$. An estimate of exchange parameters corresponding to the population of the excited state and the rate of exchange between interconverting states (p_E, k_{ex}), was not attempted due to ^{1}H–^{1}H cross-relaxation effects (Yuwen et al. 2017b). It is worth noting, however, that for cases where cross-relaxation is negligible, so that isolation of exchange parameters can be achieved, the relative short recycle delay (d_1) used for the amide experiment is not problematic as longitudinal relaxation during the course of the pulse scheme is taken into account in the

analysis. The optimal value for $d_1 + T_{Ex}$ in terms of maximal signal-to-noise in this case depends on the amide ^{1}H R_1 relaxation rates that can vary depending on exchange with water, for example. We have shown previously that for $R_1 \sim 2$ s^{-1} a value of $d_1 + T_{Ex} \sim 1$ s is optimal (Yuwen and Kay 2017), similar to what has been used here, but it may well be that for a deuterated sample with slower rates a larger d_1 value would be preferable.

Results and discussion

A new class of experiment where the magnetization of interest before and after the CEST element is distinct

Figure 1a illustrates schematically the essential element of a CEST experiment. It consists of a period of fixed duration during which longitudinal magnetization (Vallurupalli et al. 2012) or two-spin order (Sekhar et al. 2016) is allowed to evolve in the presence of a weak radio-frequency field (typically 10–50 Hz) that is applied over a range of frequencies, one frequency, ω_1, per experiment. In all biomolecular NMR applications that we are aware of the magnetization at the start of the CEST period is also the magnetization that is selected at the end of the relaxation period. Thus, magnetization of the form O_z at $t=0$ becomes $a(\omega_1)O_z$ at $t=T_{Ex}$, where O_z is the operator of interest, and per-residue $a(\omega_1)$ values are subsequently 'read out' via the intensities of cross-peaks in the resulting spectra. A series of spectra are recorded, each with a different ω value to generate the characteristic CEST profile, $a(\omega)$, that is then analyzed to extract exchange parameters and chemical shifts of nuclei in the sparsely populated state (Vallurupalli et al. 2017). A particular case that is of relevance to the discussion that follows is illustrated in Fig. 1b in which a pair of simulated spin-state selective ^{1}H CEST profiles is shown for an amide ^{1}H coupled to its attached ^{15}N spin in either the up (α) or down (β) state. As described previously, the CEST major and minor dips are offset in each profile by $^1J_{NH}$, the one-bond ^{1}H–^{15}N scalar coupling (Yuwen et al. 2017b). In contrast, so called NOE dips that result from dipolar coupling of the amide proton of interest with a proximal amide proton spin are not offset so that in the difference spectrum these dips are completely removed. The process of subtracting the spin-state selective profiles is equivalent to selecting longitudinal order at the end of the CEST element. This can be seen, qualitatively, by noting that the magnetization of interest in each of the ^{15}N spin up or spin down experiments is given by I_zN^α and I_zN^β, respectively, where I_z corresponds to ^{1}H z magnetization while N^j denotes the ^{15}N spin-state ($j \in \{\alpha, \beta\}$), so that the difference is thus $I_zN^\alpha - I_zN^\beta = 2I_zN_z$. More formally, starting

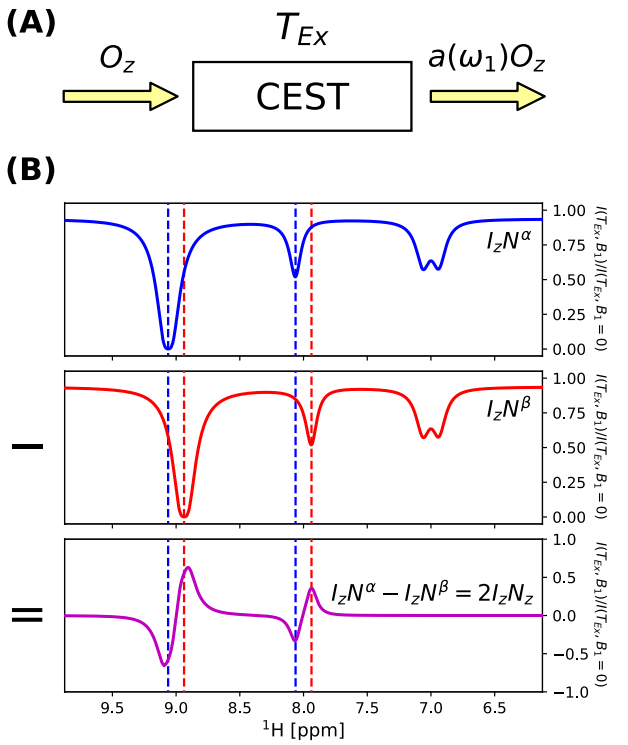

Fig. 1 **a** In a typical CEST experiment magnetization of the form O_z at the start of the CEST element is selected at the end of the relaxation period of duration T_{Ex}. Application of the weak B_1 field can affect the magnitude of O_z in a manner that depends on the position of the field and the resonance frequencies of ground and excited state spins (Vallurupalli et al. 2017). A plot of $a(\omega)$ versus ω, where ω is the frequency of application of the weak B_1 field, is referred to as a CEST profile. **b** Schematic of spin-state selective amide ^{1}H CEST curves derived from ^{1}H magnetization coupled to the attached ^{15}N spin in the α (*blue*, I_zN^α) or β (*red*, I_zN^β) spin-state, along with the difference profile (*magenta*, $I_zN^\alpha - I_zN^\beta$). Note that both spin-state CEST profiles are normalized with respect to intensities of peaks obtained with $B_1 = 0$ during the CEST element, as indicated by the y-axis labels

from ^{1}H magnetization prior to the CEST element that then evolves during the CEST period, we can write

$$\frac{1}{2}I_z(1+2N_z) + \frac{1}{2}I_z(1-2N_z) \xrightarrow{CEST} a(\omega)\frac{1}{2}I_z(1+2N_z) + b(\omega)\frac{1}{2}I_z(1-2N_z) \quad (1)$$

Here we have explicitly included both of the ^{1}H multiplet components, with the evolution of magnetization during the CEST element taken into account via the coefficients $a(\omega)$ and $b(\omega)$ that are the intensities of each of the spin-state components after CEST. When the position of the weak B_1 CEST field is far removed from either ground or excited state resonance positions $a(\omega) = b(\omega)$ since there is no effect on ^{1}H longitudinal magnetization. Conversely, when the field is applied at the resonance frequency of the excited state amide proton of interest coupled to the down ^{15}N spin position,

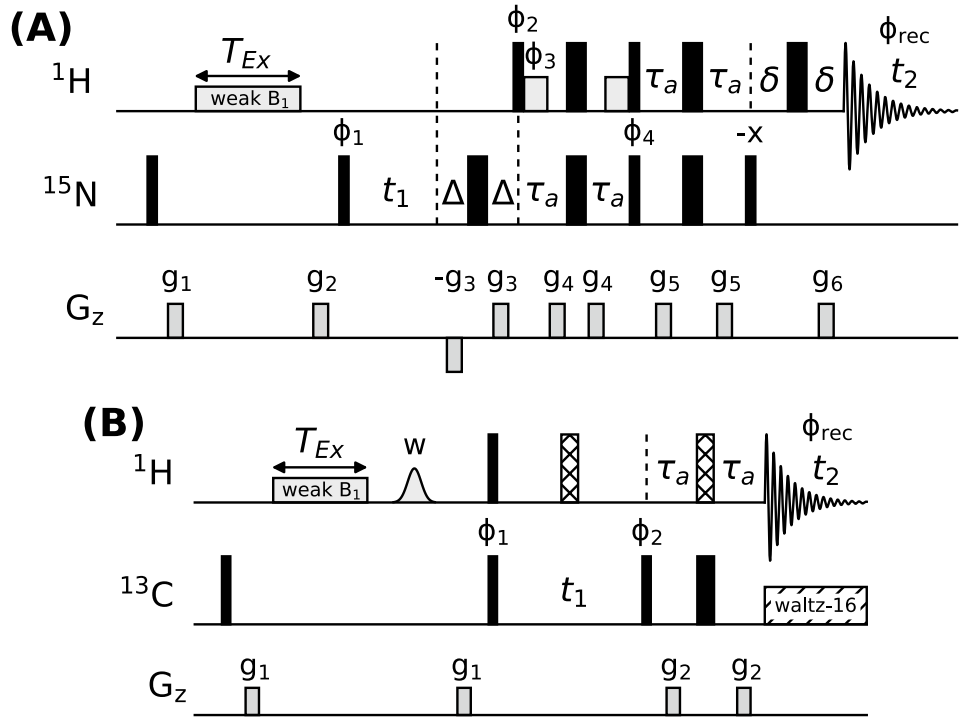

Fig. 2 **a** TROSY version of the amide ^{1}H CEST experiment where longitudinal order is selected immediately after the CEST element. 90° (180°) rectangular pulses on ^{1}H and ^{15}N channels, denoted by *narrow* (*wide*) *black rectangles*, are applied at maximum power. Water-selective rectangular pulses (*grey*) typically have durations of ~2 ms. The ^{1}H carrier is set at the position of water (~4.7 ppm) except during the CEST element where it is placed in the amide ^{1}H region of the spectrum (1 frequency/2D spectrum), while the ^{15}N carrier is at the center of the amide ^{15}N spectral region (~119 ppm). Values of the delays are: $\tau_a \simeq 1/(4^1J_{HN}) = 2.68$ ms, $\Delta = 850$ µs, $\delta = 500$ µs. All pulses are applied with phase x unless otherwise indicated. The following phase cycle is used: ϕ_1 = y, −y, −x, x; ϕ_2 = y; ϕ_3 = −y; ϕ_4 = −y; ϕ_{rec} = −y, y, −x, x. Quadrature detection in F_1 is achieved by inverting the phases of ϕ_2, ϕ_3, ϕ_4, ϕ_{rec} together with the sign of gradient g_6 (Kay et al. 1992; Schleucher et al. 1993) and changing ϕ_1 to y, −y, x, −x. A minimum four step cycle is recommended for optimal TROSY selection, however two steps is sufficient since coherence selection gradients (g_3, g_6) are applied. Gradients are applied with the following durations (ms) and strengths (in % maximum): g_1: (0.4, −25%), g_2: (1.0, 15%), g_3: (0.625, 80%), g_4: (0.256, 60%), g_5: (0.256, 15%), g_6: (0.256, −39.6%). The weak ^{1}H B_1 field was calibrated using the approach of Guenneugues et al. (1999) It is worth noting that the phase cycle selects both ^{15}N longitudinal magnetization and two-spin order that is present at the end of the CEST element and both components are ultimately detected. However, as ^{15}N longitudinal magnetization is destroyed immediately prior to the CEST element via the 90° pulse–g_1 gradient pair and only recovers for delay T_{Ex}, while signal from it is proportional to the ^{15}N gyromagnetic ratio γ_N and not γ_H, the contribution is small; as discussed in the text, the net effect is a slight baseline offset. A similar effect does not occur in the methyl-TROSY scheme as ^{13}C longitudinal magnetization at the end of the CEST period is not transferred to observable signal. **b** Methyl-TROSY based ^{1}H CEST experiment. 90° (180°) rectangular pulses on ^{1}H and ^{13}C channels, denoted by *narrow* (*wide*) *black rectangles*, are applied at maximum power. The *hatched bars* denote $90_y180_x90_y$ composite pulses (Levitt and Freeman 1979) and the water-selective shaped pulse marked with "w" (~7 ms) uses the EBURP-1 profile (Geen and Freeman 1991) The ^{1}H carrier is set to the center of methyl group region (~0.5 ppm) except during the CEST element where it is placed at the desired frequency, while the ^{13}C carrier is positioned at the center of the methyl ^{13}C spectral region (~20 ppm). ^{13}C WALTZ-16 decoupling (Shaka et al. 1983) is applied with a field of ~2 kHz. The delay $\tau_a \simeq 1/(4^1J_{HC}) = 2.00$ ms. All pulses are applied with phase x unless otherwise indicated. The following phase cycle is used: ϕ_1 = x, −x; ϕ_2 = 2(x), 2(−x); ϕ_{rec} = x, −x, −x, x with a minimum phase cycle of 2. Quadrature detection in F_1 is achieved by shifting the phase of ϕ_1 by π/2. Gradients are applied with the following durations (ms) and strengths (in % maximum): g_1: (1.0, 50%), g_2: (0.5, 40%). An alternative scheme implements the 3-9-19 WATERGATE element (Sklenar et al. 1993) during the final INEPT period to achieve much higher water suppression for applications to proteins dissolved in H_2O; a stronger pair of g_2 gradients, g_2: (0.8, 80%), should then be applied

$I_z^E(1 - 2N_z^E)$, where the superscript E explicitly indicates that an excited state resonance is affected, the perturbation of magnetization is transferred selectively to $I_z(1 - 2N_z)$ of the ground state and $a(\omega) > b(\omega)$. In a spin-state selective ^{1}H CEST experiment the separate pathways corresponding to the transfer of $I_z(1 \pm 2N_z)$ to observable magnetization are recorded individually and the profiles $a(\omega)$ and $b(\omega)$ subtracted subsequently (Yuwen et al. 2017b). However, a simpler approach is possible, as suggested by the above discussion. If immediately after the CEST element longitudinal order, $2I_zN_z$, rather than ^{1}H longitudinal magnetization is selected (Fig. 2, phase ϕ_1), then the subtraction $a(\omega) - b(\omega)$

is done 'on the fly', obviating the need for lengthy spin-state selective pulse schemes. Thus, in the context of the CEST element, the input and output coherences are distinct. This offers a number of advantages for recording ^{1}H CEST based experiments that are free from NOE artifacts, as detailed below.

Experimental applications

Figure 2a, b illustrate a pair of TROSY-based pulse schemes for recording amide and methyl proton CEST spectra, respectively, that exploit the selection of longitudinal order immediately after the CEST element. In principle, a number of advantages over our previously published spin-state selective experiments are anticipated. These include: (i) increased sensitivity, since the number of transfer steps is significantly reduced; (ii) only a single dataset is required, rather than separate spectra for each of the spin-state selective pathways, decreasing measurement time in many cases; (iii) because the difference operation ($a(\omega)-b(\omega)$) is effectively performed immediately after the CEST element, relaxation effects past this point do not compromise the experiment. This is unlike the case for experiments in which additional steps in the sequence are required to facilitate the separation of spin-state selective pathways where relaxation, pulse imperfections and slight missets of transfer times can in some cases lead to 'contamination' of the pathways (see below); (iv) ^{1}H CEST experiments that use unenhanced HSQC schemes as a 'read out' can be readily designed with the present approach. Such implementations are potentially very useful in studies of systems with either fast transverse relaxation (Sekhar et al. 2016) or fast solvent exchange (Yuwen and Skrynnikov 2014). Although only a pair of examples is illustrated here it is possible to readily incorporate this approach into all existing ^{1}H CEST experiments.

In order to illustrate the advantages of the pulse schemes of Fig. 2 over their spin-state selective counterparts (Yuwen et al. 2017b) we have recorded comparative datasets on [U-^{15}N; U-^{2}H]- ($^{1}H^{N}$) and [U-^{15}N; U-^{2}H; Ileδ1-$^{13}CH_3$; Leu,Val-$^{13}CH_3$/$^{12}CD_3$; Met-$^{13}CH_3$]- (^{1}H methyl) L99A T4L samples. Mutation of Leu to Ala at position 99 in T4 lysozyme results in the formation of a 150 Å^3 cavity (Eriksson et al. 1992) that is accessible to Phe 114 via an exchange process that has been characterized in detail previously using relaxation dispersion NMR methods (Bouvignies et al. 2011; Mulder et al. 2001). The exchange rate varies significantly with temperature and at approximately 10 °C the exchange time-scale is such that high quality CEST profiles can be easily recorded (Yuwen et al. 2017b). Figure 3 shows representative CEST curves obtained directly from measurements using the scheme of Fig. 2a (*green*) or from the difference of spin-state profiles, as described previously (*magenta*) (Yuwen et al. 2017b), recorded at 8.8 °C, 800 MHz, where the assumed isotropic correlation time of L99A T4L is approximately 19 ns. The resonance positions of protons with coupled amide ^{15}N spins in either α or β spin-states are indicated by the *dashed blue* and *red lines*, respectively. Datasets were recorded for equivalent measurement times and the resulting profiles normalized so that the noise floors are the same. Notably, the sensitivity of the current scheme is superior to our previous method by, on average, a factor of 1.56 ± 0.26 and 1.50 ± 0.30, for the major and minor dips, respectively. In the analysis the intensity of an anti-phase dip was quantified as the difference in intensities between maxima and minima in each lineshape. Finally, a linear correlation plot of the extracted ^{15}N chemical shift differences between exchanging spins in ground and excited states, $\Delta\varpi_{GE}$ ($=\varpi_E-\varpi_G$), obtained from fits of the difference CEST profiles generated via spin-state selection or the pulse scheme of Fig. 2a is shown in panel F, where it is clear that excellent agreement is obtained.

Of interest, baselines for the most part slightly deviate from zero for profiles generated from the new approach (Fig. 3), while those for the difference profiles obtained from the spin-state selective experiments do not. The non-zero baselines can be understood by noting that the longitudinal relaxation rates of the individual multiplet components are not identical due to cross-correlated spin relaxation between ^{1}H–^{15}N dipolar and ^{1}H chemical shift anisotropy (CSA) interactions (Goldman 1984). Thus, even when the weak B_1 CEST field is distal from the resonance positions of either major or minor state peaks there is a slight imbalance between intensities of multiplet components due to differential relaxation during the CEST element so that $a(\omega)\neq b(\omega)$, leading to a non-zero baseline. This same phenomenon occurs in the spin-state selective experiment as well but in that case because individual profiles are obtained prior to subtraction the difference can be normalized out. This is most simply accomplished by recording separate reference planes for each of the ^{1}H multiplet components, I_zN^j $j\in\{\alpha,\beta\}$, where the B_1 field is turned off during the CEST delay so that the intensity ratio of cross peaks, $I(T_{Ex},B_1)/I(T_{Ex},B_1=0)$, 'subtracts' out this effect (Yuwen et al. 2017b). A second contributing factor to the baseline offset derives from the fact that a small amount of ^{15}N magnetization recovers from zero during the CEST element. It is subsequently transferred to observable ^{1}H signal via the TROSY-scheme of Fig. 2a, along with the desired longitudinal order. As magnetization from a given ^{15}N spin is not modulated by the position of the weak ^{1}H B_1 field during T_{Ex}, at least when it is applied off-resonance from the attached amide proton in question so that the heteronuclear NOE can be neglected, the net effect is the introduction of a constant offset to $I(T_{Ex},B_1)$. It is worth noting that signal derived from ^{15}N scales as γ_N, as opposed

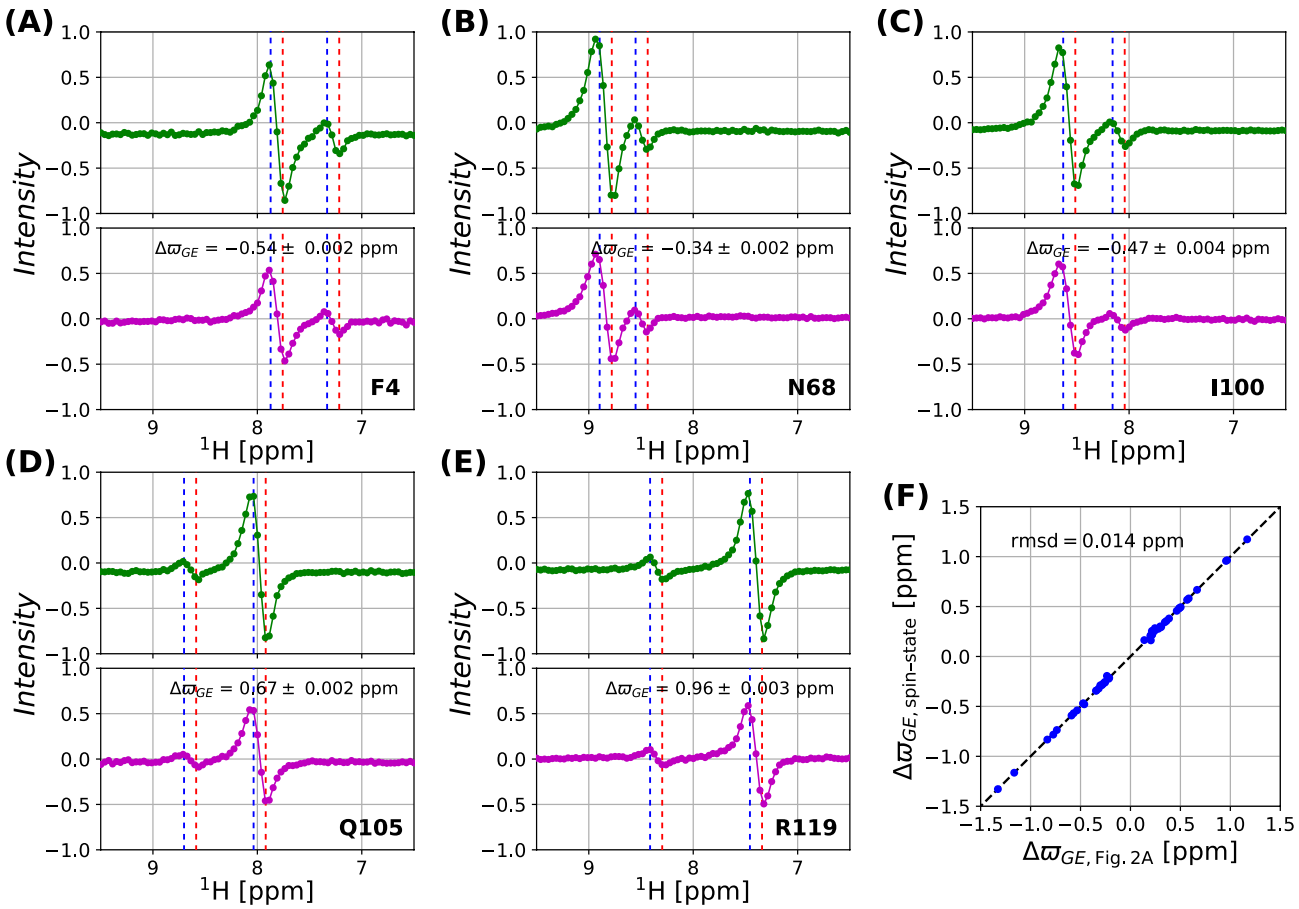

Fig. 3 Representative amide ^{1}H CEST profiles measured with the scheme of Fig. 2a (*top*; y-axis intensity = $I(T_{Ex},B_1)/I_{HSQC}$, scaled so that the intensity range extends from −1 to 1) and via spin-state selection (*bottom*; y-axis intensity = $I(T_{Ex},B_1)/I(T_{Ex},B_1=0)$) (Yuwen et al. 2017b) recorded on a L99A T4L sample, 8.8 °C, 800 MHz, T_{Ex} = 400 ms, weak B_1 field = 30.4 Hz (**a**–**e**). Positions of ground and excited state chemical shifts are indicated by *red* (TROSY-, ^{15}N spin β) and *blue* (anti-TROSY-, ^{15}N spin α) *dashed lines*. The two sets of ^{1}H CEST profiles have been rescaled such that the noise levels are the same. **f** Correlation plot of $\Delta\varpi_{GE}$ values from the spin-state selective experiment (Yuwen et al. 2017b), y-axis, and the scheme of Fig. 2a, x-axis

to the signal from longitudinal order that is proportional to γ_H, so that the offset is expected to be small.

Figure 4 shows a number of methyl-TROSY based ^{1}H CEST profiles from datasets recorded on L99A T4L, 8.8 °C, 800 MHz, with resonance positions of ^{1}H multiplet components corresponding to α and β spin-states of the coupled ^{13}C spin indicated by *blue* and *red dashed lines*, respectively. Here the sensitivity gains with the new approach are even larger than for the amide experiment, with average gains of 2.25 ± 0.45 and 2.36 ± 0.70-fold, for the major and minor dips, respectively (see below). Notably, the baselines of profiles are not displaced in this application as (i) average methyl ^{1}H CSA values are small, with $\Delta\sigma$ typically on the order of 1 ppm (Tugarinov et al. 2004) and (ii) the small amount of ^{13}C longitudinal magnetization that recovers during the CEST element cannot be transferred into observable ^{1}H signal from the remaining portion of the pulse scheme. Of interest, additional minor dips are noted for a number of the residues, such as M106, that derive from a third minor state that has been observed previously in amide ^{1}H dispersion experiments recorded at 25 °C involving residues 135–150 and additional amino acids that contact them, such as M106. A linear correlation plot of extracted $\Delta\varpi_{GE}$ values via the scheme of Fig. 2b and the corresponding spin-state selective experiment is illustrated in panel F, showing that the agreement is excellent.

A comparison of the corresponding CEST profiles measured using the spin-state selective experiments described previously (Yuwen et al. 2017a) and the present versions, readily establishes the sensitivity gains that can be obtained with the schemes of Fig. 2. The expected relative sensitivities of the experiments, neglecting the effects of spin relaxation and assuming perfect pulses, can be understood by considering the magnetization transfer pathways operative in each scheme. For example, in the pulse sequence of Fig. 2a (amide-TROSY) the magnetization transfer is given by

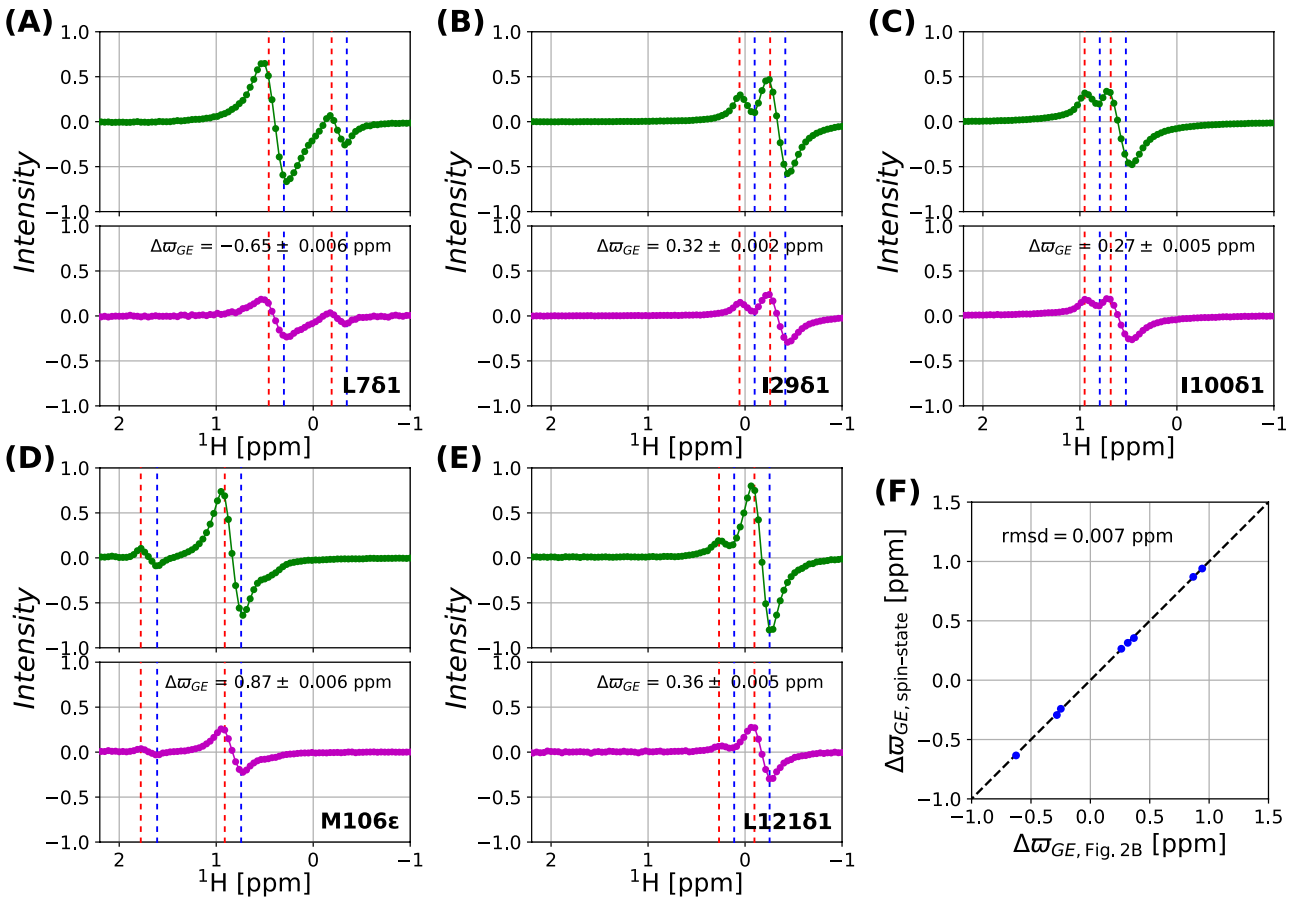

Fig. 4 Representative methyl ^{1}H CEST profiles measured with the scheme of Fig. 2b (*top*; intensity = $I(T_{Ex},B_1)/I_{HMQC}$, scaled so that the intensity range extends from −1 to 1) and the spin-state selective approach (*bottom*; y-axis intensity = $I(T_{Ex},B_1)/I(T_{Ex},B_1=0)$) (Yuwen et al. 2017a) (**a**–**e**). A $^{13}CH_3$-labeled L99A T4L sample was used, 8.8 °C, 800 MHz, T_{Ex} = 500 ms, weak B_1 field = 30.6 Hz. The two sets of ^{1}H CEST profiles have been rescaled such that the noise levels are the same. The additional minor dip near the ground state position of M106ε (panel D) likely derives from a third state involved in an additional slow exchange process. **f** Correlation plot of $\Delta\varpi_{GE}$ values extracted via the spin-state selective approach (Yuwen et al. 2017a) and the scheme of Fig. 2b

$$\begin{aligned}&\frac{1}{2}I_z(1+2N_z)+\frac{1}{2}I_z(1-2N_z)\xrightarrow{CEST}a(\omega)\frac{1}{2}I_z(1+2N_z)+b(\omega)\frac{1}{2}I_z(1-2N_z)\xrightarrow{\phi_1,\phi_{rec}}\frac{a(\omega)-b(\omega)}{2}2I_zN_z\\&=\frac{a(\omega)-b(\omega)}{4}\{N_z(1+2I_z)-N_z(1-2I_z)\}\xrightarrow{TROSY\ filter}\frac{a(\omega)-b(\omega)}{4}I_{TR}(1-2N_z)\end{aligned}\tag{2}$$

where we have written the TROSY and anti-TROSY components explicitly, as in Eq. 1, and selected only those terms proportional to N_z after the CEST element (i.e., $2I_zN_z$), as indicated by ϕ_1, ϕ_{rec} over the arrow pointing to $2I_zN_z$. After $2N$ scans the resultant signal is $0.5N\{a(\omega)-b(\omega)\}$ and the noise floor is $(2N)^{1/2}$. Recall that the experiment is repeated for different ω values and the intensity of cross-peaks in 2D spectra quantified to generate the corresponding CEST profile. In contrast, using our previous approach (Yuwen et al. 2017b) anti-TROSY and TROSY components, derived from the $a(\omega)\frac{1}{2}I_z(1+2N_z)$ and $b(\omega)\frac{1}{2}I_z(1-2N_z)$ terms in Eq. 2, are selected in separate scans to generate spin-state selective CEST profiles with intensities proportional to $a(\omega)/2$ and $b(\omega)/2$, respectively. The difference CEST profile, from $2N$ scans, is thus given by $0.5N\{a(\omega)-b(\omega)\}$, where we note that N scans are used to record each of the spin-state selective pathways. Thus, the signal-to-noise in both classes of experiment is predicted to be the same under the assumptions given above.

A similar analysis of magnetization transfer in the methyl-TROSY based scheme of Fig. 2b shows that

$$\begin{aligned}
&\frac{1}{2}I_z(1+2C_z)+\frac{1}{2}I_z(1-2C_z)\\
&\xrightarrow{CEST} a(\omega)\frac{1}{2}I_z(1+2C_z)+b(\omega)\frac{1}{2}I_z(1-2C_z)\\
&\xrightarrow{\phi_1,\phi_{rec}} \frac{a(\omega)-b(\omega)}{2}2I_zC_z \xrightarrow{INEPT} \frac{a(\omega)-b(\omega)}{2}I_{TR}
\end{aligned} \tag{3}$$

Thus after $2N$ scans the resultant signal is $N\{a(\omega)-b(\omega)\}$ and the noise floor is $(2N)^{1/2}$. In contrast, an analogous spin-state selective experiment (Yuwen et al. 2017a) separates the TROSY and anti-TROSY pathways by addition and subtraction using an IP/AP type approach (Ottiger et al. 1998; Yang and Nagayama 1996). Here magnetization immediately prior to acquisition is given as $a(\omega)\frac{1}{2}I_{TR}(1+2C_z)+b(\omega)\frac{1}{2}I_{TR}(1-2C_z)$ (data set 1) and as $a(\omega)\frac{1}{2}I_{TR}(1+2C_z)-b(\omega)\frac{1}{2}I_{TR}(1-2C_z)$ (data set 2). Addition and subtraction of the resultant datasets gives new spectra, denoted as $a(\omega)I_{TR}(1+2C_z)$ and $b(\omega)I_{TR}(1-2C_z)$, respectively, with the difference CEST profile calculated as the difference in corresponding peak intensities in these two sets of spectra as a function of ω. It is straightforward to show that after $2N$ scans the intensity of the difference CEST profile is $N\{a(\omega)-b(\omega)\}$ but that the resultant noise floor is $2N^{1/2}$, that is $\sqrt{2}$ higher than in the experiment of Fig. 2. The increased noise floor in the spin-state based scheme derives from the fact that decoupling during acquisition cannot be employed in that case. Thus, the sequence of Fig. 2b is calculated to generate profiles that are $\sqrt{2}$ higher in signal-to-noise than the corresponding spin-state selective approach.

Figures 3 and 4 shows that there are quite clearly additional gains beyond those that might be anticipated on the basis of the theoretical arguments given above. Such gains likely reflect, in part, the inherent difficulties in isolating spin-state selective pathways in the spin-state selective experiments. For example, in the case of the methyl-TROSY spin-state CEST experiment differential relaxation between elements that are combined to produce the required spin-state selective components effectively leads to leakage from one pathway to the next. Although this has no effect on the position of the dips in the difference CEST profile it does result in an intensity loss and hence a relative intensity gain for the new class of experiment described here. An additional factor that contributes to the sensitivity gain is that the sequences of Fig. 2 are considerably shorter than their spin-state counterparts, as mentioned above, that is important in applications to biomolecules.

Central to the utility of any ^{1}H-based CEST experiment is the removal of NOE dips whose appearance would otherwise complicate interpretation of the data (Bouvignies and Kay 2012b). As illustrated in Fig. 1, this is accomplished in the spin-state class of experiment by subtraction of individual CEST profiles that have identical contributions from cross-relaxation (Yuwen et al. 2017b). In the case of the pulse schemes of Fig. 2, where longitudinal order is selected immediately after the CEST element, elimination of the NOE dips occurs automatically. This can be readily appreciated by considering the evolution of magnetization during the CEST element, focusing exclusively on the effects of cross-relaxation for the moment. Suppose that the weak B_1 CEST field is applied at the resonance frequency of an amide proton spin that is proximal to the amide spin of interest (I). Since both I spin multiplet components are affected equally by cross-relaxation, $a(\omega)$ and $b(\omega)$ in Eq. 1 are equal and there is no contribution to the detected term $2I_zN_z$. An

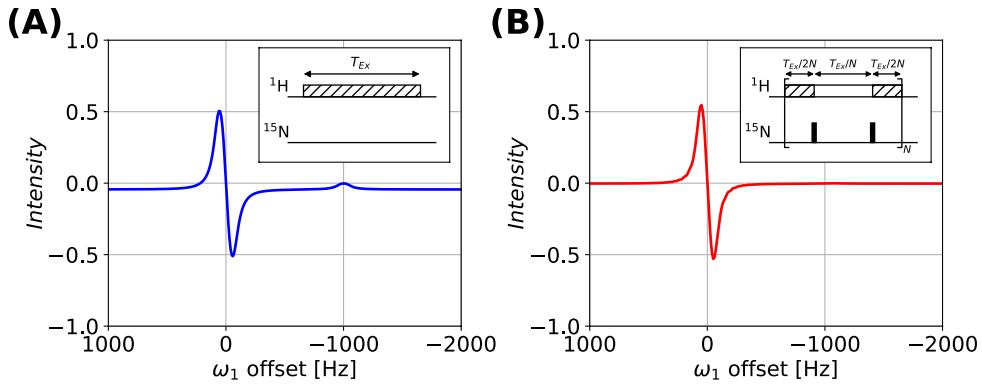

Fig. 5 **a** Numerical simulation illustrating a potential artifact introduced through the interplay between ^{1}H–^{15}N dipolar, ^{1}H CSA cross-correlation and ^{1}H–^{1}H cross-relaxation effects. The simulation was based on the following parameters: ^{1}H longitudinal cross-correlation rate $\eta_z=0.1$ s^{-1}, ^{1}H–^{1}H cross relaxation rate $\sigma=-10$ s^{-1}, $T_{Ex}=500$ ms, B_1 (CEST)$=30$ Hz, $^1J_{HN}=-93$ Hz. B_1 inhomogeneity has been taken into account as described previously (Vallurupalli et al. 2012). The ground state and NOE dips are located at 0 and -1000 Hz respectively. **b** The modified ^{1}H CEST element (*inset*, $N=2$ is used for the simulation) eliminates cross-correlated spin-relaxation over the complete duration of the CEST interval so that NOE dips are removed. Note, however, that we have not observed any NOE dips experimentally when the simple CEST scheme as indicated in the **a** *inset* is used

assumption is that both I spin multiplet components have equivalent R_1 relaxation rates, a condition that is not be completely fulfilled when dipolar–CSA cross-correlation effects are non-zero (Goldman 1984). In this case the NOE contributions do not completely subtract, as can be readily seen from Fig. 1b if one adds slightly different offsets to the CEST baselines for the individual spin-state components. This is not an issue when separate spin-state selective experiments are recorded because, as described above, differences in R_1 relaxation rates are 'normalized out' by recording separate reference planes (Yuwen et al. 2017b). Figure 5a illustrates this scenario for a CEST profile simulated with the scheme of Fig. 2 assuming a ^{1}H–^{1}H cross-relaxation rate of -10 s^{-1} and a ^{1}H longitudinal dipolar/CSA cross-correlation relaxation rate of 0.1 s^{-1}, close to the maximum value that can be achieved (~0.14 s^{-1}, when molecular tumbling is described by a single correlation time such that $\tau_c = 1/\omega_H$, where ω_H is the Larmor frequency of a ^{1}H spin). This value is calculated assuming an axially symmetric ^{1}H^N CSA tensor with $\Delta\sigma = 10$ ppm whose principle axis is collinear with the ^{1}H–^{15}N bond (Tjandra and Bax 1997). In this case the inequality in longitudinal relaxation rates can be compensated using the scheme illustrated in the inset to Fig. 5b, where individual CEST elements of duration T_{Ex}/N are separated by periods of length T_{Ex}/N during which the CEST field is not applied, and where the multiplet components are interchanged. The resulting simulated profile shows that the small NOE dip is eliminated. Note that for macromolecules such as proteins, ^{1}H longitudinal cross-correlated relaxation depends on the spectral density term $J(\omega_H)$, while ^{1}H–^{1}H cross-relaxation is dominated by a term of the form $J(0)$ (Cavanagh et al. 2007) Since $J(\omega_H)$ is proportional to $1/(\omega_H^2\tau_c)$ for a rigid amide group while $J(0)$ is proportional to τ_c, it is rare to have systems with significant cross-relaxation *and* cross-correlation, so that these artifacts are predicted to be small. It is worth noting that we have seen no evidence of NOE dips in any experiments that we have recorded using the new schemes, over a temperature range extending from 4 to 25 °C, even at the smallest field that we currently have in our laboratory (500 MHz) where the difference in ^{1}H longitudinal relaxation rates from dipolar–CSA cross-correlation is predicted to be largest. The potential for incomplete subtraction of NOE dips is thus more of an interesting nuance than a practical concern. As an aside, an additional benefit of the scheme which suppresses cross-correlated relaxation during the CEST element is that, to good approximation, there is little buildup of ^{15}N longitudinal magnetization by the end of T_{Ex} as pairs of ^{15}N 180° pulses that invert z-magnetization are applied equidistantly. This further eliminates any baseline offset (see above).

Concluding remarks

We have presented examples of ^{1}H CEST-based experiments that suppress dipolar cross-relaxation 'on the fly' so as to produce clean profiles that can be analyzed to robustly extract chemical shifts of excited state ^{1}H spins. Notably, unlike other CEST schemes, the ones presented here select longitudinal magnetization before the CEST element and longitudinal order immediately after it, leading to significant sensitivity gains relative to previously introduced spin-state selective experiments that rely on the evolution of longitudinal magnetization throughout the CEST element (Yuwen et al. 2017a, b; Yuwen and Kay 2017). It is anticipated that these CEST experiments will serve as useful additions to the NMR toolkit for studies of conformationally excited states. Further, the realization that in some cases it may be beneficial to select elements at the end of the CEST relaxation interval that are distinct from those at the beginning may serve to stimulate new and improved implementations of this methodology.

Acknowledgements This work was supported by grants from the Canadian Institutes of Health Research (CIHR) and the Natural Sciences and Engineering Research Council of Canada. T.Y. acknowledges post-doctoral support from the CIHR. L.E.K. holds a Canada Research Chair in Biochemistry. Valuable discussions with Dr. Ashok Sekhar are acknowledged.

References

Bouvignies G, Kay LE (2012a) A 2D ^{13}C-CEST experiment for studying slowly exchanging protein systems using methyl probes: an application to protein folding. J Biomol NMR 53:303–310. https://doi.org/10.1007/s10858-012-9640-7

Bouvignies G, Kay LE (2012b) Measurement of proton chemical shifts in invisible states of slowly exchanging protein systems by chemical exchange saturation transfer. J Phys Chem B 116:14311–14317. https://doi.org/10.1021/jp311109u

Bouvignies G et al (2011) Solution structure of a minor and transiently formed state of a T4 lysozyme mutant. Nature 477:111–114. https://doi.org/10.1038/nature10349

Bouvignies G, Vallurupalli P, Kay LE (2014) Visualizing side chains of invisible protein conformers by solution NMR. J Mol Biol 426:763–774. https://doi.org/10.1016/j.jmb.2013.10.041

Cavanagh J, Fairbrother WJ, Palmer AG, Rance M, Skelton N (2007) Protein NMR spectroscopy, 2 edn. Academic Press, London

Delaglio F, Grzesiek S, Vuister GW, Zhu G, Pfeifer J, Bax A (1995) NMRPipe: a multidimensional spectral processing system based on Unix pipes. J Biomol NMR 6:277–293. https://doi.org/10.1007/Bf00197809

Eriksson AE, Baase WA, Wozniak JA, Matthews BW (1992) A cavity-containing mutant of T4 lysozyme is stabilized by buried benzene. Nature 355:371–373. https://doi.org/10.1038/355371a0

Fawzi NL, Ying JF, Ghirlando R, Torchia DA, Clore GM (2011) Atomic-resolution dynamics on the surface of amyloid-beta protofibrils probed by solution NMR. Nature 480:268–272. https://doi.org/10.1038/nature10577

Forsen S, Hoffman RA (1963) Study of moderately rapid chemical exchange reactions by means of nuclear magnetic double resonance. J Chem Phys 39:2892–2901. https://doi.org/10.1063/1.1734121

Geen H, Freeman R (1991) Band-selective radiofrequency pulses. J Magn Reson 93:93–141. https://doi.org/10.1016/0022-2364(91)90034-Q

Goldman M (1984) Interference effects in the relaxation of a pair of unlike spin-1/2 nuclei. J Magn Reson 60:437–452. https://doi.org/10.1016/0022-2364(84)90055-6

Guenneugues M, Berthault P, Desvaux H (1999) A method for determining B_1 field inhomogeneity. Are the biases assumed in heteronuclear relaxation experiments usually underestimated? J Magn Reson 136:118–126. https://doi.org/10.1006/jmre.1998.1590

Hansen AL, Bouvignies G, Kay LE (2013) Probing slowly exchanging protein systems via $^{13}C^{\alpha}$-CEST: monitoring folding of the Im7 protein. J Biomol NMR 55:279–289. https://doi.org/10.1007/s10858-013-9711-4

Ishima R, Baber J, Louis JM, Torchia DA (2004) Carbonyl carbon transverse relaxation dispersion measurements and ms-μs timescale motion in a protein hydrogen bond network. J Biomol NMR 29:187–198. https://doi.org/10.1023/B:JNMR.0000019249.50306.5d

Kay LE, Keifer P, Saarinen T (1992) Pure absorption gradient enhanced heteronuclear single quantum correlation spectroscopy with improved sensitivity. J Am Chem Soc 114:10663–10665. https://doi.org/10.1021/ja00052a088

Levitt MH, Freeman R (1979) NMR population-inversion using a composite pulse. J Magn Reson 33:473–476. https://doi.org/10.1016/0022-2364(79)90265-8

Mulder FAA, Mittermaier A, Hon B, Dahlquist FW, Kay LE (2001) Studying excited states of proteins by NMR spectroscopy. Nat Struct Biol 8:932–935. https://doi.org/10.1038/nsb1101-932

Ottiger M, Delaglio F, Bax A (1998) Measurement of J and dipolar couplings from simplified two-dimensional NMR spectra. J Magn Reson 131:373–378. https://doi.org/10.1006/jmre.1998.1361

Palmer AG, Kroenke CD, Loria JP (2001) Nuclear magnetic resonance methods for quantifying microsecond-to-millisecond motions in biological macromolecules. Methods Enzymol 339:204–238. https://doi.org/10.1016/S0076-6879(01)39315-1

Rennella E, Huang R, Velyvis A, Kay LE (2015) $^{13}CHD_2$-CEST NMR spectroscopy provides an avenue for studies of conformational exchange in high molecular weight proteins. J Biomol NMR 63:187–199. https://doi.org/10.1007/s10858-015-9974-z

Schleucher J, Sattler M, Griesinger C (1993) Coherence selection by gradients without signal attenuation: application to the three-dimensional HNCO experiment. Angew Chem Int Ed 32:1489–1491. https://doi.org/10.1002/anie.199314891

Sekhar A, Rosenzweig R, Bouvignies G, Kay LE (2016) Hsp70 biases the folding pathways of client proteins. Proc Natl Acad Sci USA 113:E2794–E2801. https://doi.org/10.1073/pnas.1601846113

Shaka AJ, Keeler J, Frenkiel T, Freeman R (1983) An improved sequence for broadband decoupling: WALTZ-16. J Magn Reson 52:335–338. https://doi.org/10.1016/0022-2364(83)90207-X

Sklenar V, Piotto M, Leppik R, Saudek V (1993) Gradient-tailored water suppression for $^{1}H–^{15}N$ HSQC experiments optimized to retain full sensitivity. J Magn Reson Ser A 102:241–245. https://doi.org/10.1006/jmra.1993.1098

Tjandra N, Bax A (1997) Solution NMR measurement of amide proton chemical shift anisotropy in ^{15}N-enriched proteins. Correlation with hydrogen bond length. J Am Chem Soc 119:8076–8082. https://doi.org/10.1021/ja970876e

Tugarinov V, Scheurer C, Bruschweiler R, Kay LE (2004) Estimates of methyl ^{13}C and ^{1}H CSA values ($\Delta\sigma$) in proteins from cross-correlated spin relaxation. J Biomol NMR 30:397–406. https://doi.org/10.1007/s10858-004-4349-x

Vallurupalli P, Bouvignies G, Kay LE (2012) Studying "invisible" excited protein states in slow exchange with a major state conformation. J Am Chem Soc 134:8148–8161. https://doi.org/10.1021/ja3001419

Vallurupalli P, Bouvignies G, Kay LE (2013) A computational study of the effects of $^{13}C–^{13}C$ scalar couplings on ^{13}C CEST NMR spectra: towards studies on a uniformly ^{13}C-labeled protein. Chembiochem 14:1709–1713. https://doi.org/10.1002/cbic.201300230

Vallurupalli P, Sekhar A, Yuwen TR, Kay LE (2017) Probing conformational dynamics in biomolecules via chemical exchange saturation transfer: a primer. J Biomol NMR 67:243–271. https://doi.org/10.1007/s10858-017-0099-4

Yang DW, Nagayama K (1996) A sensitivity-enhanced method for measuring heteronuclear long-range coupling constants from the displacement of signals in two 1D subspectra. J Magn Reson Ser A 118:117–121. https://doi.org/10.1006/jmra.1996.0017

Yuwen T, Kay LE (2017) Longitudinal relaxation optimized amide ^{1}H-CEST experiments for studying slow chemical exchange processes in fully protonated proteins. J Biomol NMR 67:295–307. https://doi.org/10.1007/s10858-017-0104-y

Yuwen T, Skrynnikov NR (2014) CP-HISQC: a better version of HSQC experiment for intrinsically disordered proteins under physiological conditions. J Biomol NMR 58:175–192. https://doi.org/10.1007/s10858-014-9815-5

Yuwen T, Huang R, Kay LE (2017a) Probing slow timescale dynamics in proteins using methyl ^{1}H-CEST. J Biomol NMR 68:215–224. https://doi.org/10.1007/s10858-017-0121-x

Yuwen T, Sekhar A, Kay LE (2017b) Separating dipolar and chemical exchange magnetization transfer processes in ^{1}H-CEST. Angew Chem Int Ed 56:6122–6125. https://doi.org/10.1002/anie.201610759